

# The L723 low mass star forming protostellar system: resolving a double core

J. M. Girart

*Institut de Ciències de l'Espai, (CSIC-IEEC), Campus UAB, Facultat de Ciències, Torre C5 - parell 2, 08193 Bellaterra, Catalunya, Spain*

girart@ieec.cat

R. Rao

*Submillimeter Array, Academia Sinica Institute of Astronomy and Astrophysics, 645 N. Aohoku Pl, HI 9672*

rrao@sma.hawaii.edu

and

R. Estalella

*Departament d'Astronomia i Meteorologia, Universitat de Barcelona, Martí i Franquès 1, 08028 Barcelona, Catalunya, Spain*

## ABSTRACT

We present 1.35 mm Submillimeter Array (SMA) observations around the low-mass Class 0 source IRAS 19156+1906, at the center of the LDN 723 (L723) dark cloud. We detected emission from dust as well as emission from H<sub>2</sub>CO 3<sub>0,3</sub>-2<sub>0,2</sub>, DCN 3-2 and CN 2-1 lines, which arise from two cores, SMA 1 and SMA 2, separated by 2''9 (880 AU in projected distance). SMA 2 is associated with the previously detected source VLA 2. Weak SiO 5-4 emission is detected, possibly tracing a region of interaction between the dense envelope and the outflow. We modeled the dust and the H<sub>2</sub>CO emission from the two cores. The results from the modeling show that the cores have similar physical properties (density and temperature distribution) but that SMA 2 has a larger p-H<sub>2</sub>CO abundance (by a factor 3-10) than SMA 1. The p-H<sub>2</sub>CO abundances found are compatible with the value of the outer part of the circumstellar

envelopes associated with Class 0 sources. SMA 2 is harboring an active multiple low-mass protostellar system and powering at least one molecular outflow (Carrasco-González et al. 2008). In contrast, there are no known signs of outflow activity towards SMA 1. This suggests that SMA 2 is more evolved than SMA 1. The kinematics of the two sources show marginal evidence of infall and rotation motions. The mass detected by the SMA observation, which trace scales of  $\lesssim 1000$  AU, is only a small fraction of the mass contained in the large scale molecular envelope, which suggests that L723 is still in a very early phase of star formation. Despite the apparent quiescent nature of the L723, fragmentation is occurring at the center of the cloud at different scales. Thus, at  $\simeq 1000$  AU the cloud has fragmented in two cores, SMA 1 and SMA 2. At the same time, at least one of these cores, SMA 2, has undergone additional fragmentation at scales of  $\simeq 150$  AU, forming a multiple stellar system.

*Subject headings:* ISM: individual (LDN 723) — ISM: molecules — radio lines: ISM — stars: formation

## 1. Introduction

L723 is an isolated molecular cloud located at a distance of  $300 \pm 150$  pc (Goldsmith et al. 1984) and with a systemic velocity of  $V_{\text{LSR}} \simeq 10.9$  km s $^{-1}$  (Girart et al. 1997). It harbors a low-mass, Class 0, young stellar object, first identified by the IRAS satellite, IRAS 19156+1906 (Goldsmith et al. 1984), with a bolometric luminosity of  $3.4 L_{\odot}$  (Dartois et al. 2005). The properties of the protostar in the IR to mm wavelength range have been object of several studies (Davidson 1987; André, et al. 1993; Pezzuto et al. 2002; Dartois et al. 2005). IRAS 19156+1906 is associated with a CO outflow with a quadrupolar morphology (Goldsmith et al. 1984; Moriarty-Schieven & Snell 1989; Avery et al. 1990; Hayashi et al. 1991; Lee et al. 2002). This outflow consists of a pair of bipolar lobes aligned along the East–West direction (position angle  $PA \simeq 100^{\circ}$ ) and another pair of bipolar lobes aligned roughly in the North–South direction ( $PA \simeq 32^{\circ}$ ), with IRAS 19156+1906 located at their common center (Avery et al. 1990; Lee et al. 2002). The East–West (EW) pair of lobes, and in particular the blueshifted, eastern lobe, is associated with several Herbig-Haro (HH) objects (Palacios & Eiroa 1999; López et al. 2007). Very Large Array (VLA) observations at 3.6 cm reveal two sources, VLA 1 and VLA 2, toward the center of outflow (Anglada et al. 1991), although VLA 1 is likely a background source (Anglada et al. 1996; Girart et al. 1997). VLA 2 shows the characteristics of a thermal radio-jet (jet-like morphology and partially optically thick free-free emission), and was first identified as the powering source of the EW pair of

molecular lobes (Anglada et al. 1996). Recent, very sensitive, sub-arcsecond angular resolution ( $0''.2$ – $0''.7$ ) VLA observations at 3.6 cm and 7 mm resolve VLA 2 into several components. The two brightest sources at 3.6 cm, VLA 2A and 2B, are separated by  $0''.3$  (90 AU in projection) and are possibly tracing embedded protostars (Anglada 2004; Carrasco–González et al. 2008). VLA 2A is associated with extended emission along a  $PA \simeq 115^\circ$ . Two additional sources, believed to also trace embedded protostars are identified at 7 mm: VLA 2C, located at the position of the water maser emission (Girart et al. 1997; Furuya et al. 2003), and VLA 2D, located  $\sim 3''$  southeast of VLA 2A. Carrasco–González et al. (2008) suggest that the CO high velocity emission and the HH objects are tracing three different outflows. One of them is the NS outflow possibly powered by VLA 2B. The other two are what previously was considered as the EW pair of lobes: one of the outflows has a  $PA \simeq 115^\circ$  and is powered by VLA 2A, whereas the other one seems to be a “fossil” outflow with a  $PA \simeq 90^\circ$ .

High angular resolution ( $3''.5$ ) VLA observations of L723 carried out by Girart et al. (1997), show that the  $\text{NH}_3$  emission arises from a V-shaped structure that traces the dense molecular envelope around the embedded protostars. This structure is elongated roughly east-west and is 0.15 pc long, with a mass of  $7 M_\odot$ . The ammonia maps show evidence of heating and line broadening toward VLA 2. A second spot of heating is observed  $10''$  west of VLA 2. This western hot spot (WHS here after) is interpreted by Girart et al. (1997) as a very young protostar with an age shorter than  $2 \times 10^4$  yr. The  $\text{NH}_3$  structure is only partially traced by CS and  $\text{N}_2\text{H}^+$  (Hirano et al. 1998; Chen et al. 2007). The dense envelope of L723 was also observed at sub-millimeter wavelengths ( $850 \mu\text{m}$  and  $450 \mu\text{m}$ ) by Shirley et al. (2002) and Estalella et al. (2003) using the continuum SCUBA camera of the JCMT. A strong millimeter source was found, peaking at the position of VLA 2, with a large extension that matches the high-density gas traced by  $\text{NH}_3$ .

In this paper we present a study of the molecular and dust emission at scales of  $\sim 1000$  AU around the low-mass star forming region of L723. In § 2 we describe the observational procedure with the SMA. In § 3 we describe the main results obtained with the SMA data. In § 4 we present an analysis of the dust and  $\text{H}_2\text{CO}$  emission. In § 5 we discuss the possible evolutionary scenarios of the sources in the region.

## 2. SMA Observations

The observations were carried out with the 8-antenna SMA<sup>1</sup> array at Mauna Kea at 1.3 millimeters in 2004 August (compact configuration). The phase center was set at  $\alpha(J2000) = 19^{\text{h}}17^{\text{m}}53^{\text{s}}.400$  and  $\delta(J2000) = 19^{\circ}12'19''.40$ . The phase calibrator used was QSO 1925+211, and QSO 1749+096 was used as a reference calibrator. Absolute flux and band-pass calibration was done by observing Uranus and Jupiter, respectively. The SMA correlator has a bandwidth of 2 GHz with 24 partially overlapping windows (chunks) of 104 MHz. All the chunks had 128 channels, except the second chunk which was configured to have 512 channels. The correlator was setup to observe the H<sub>2</sub>CO 3<sub>0,3</sub>-2<sub>0,2</sub> line in the second chunk of the lower side band. Maps were made with the  $(u, v)$  data weighted by the associated system temperatures and using a robust weighting of 0.0 (continuum data), 0.5 (H<sub>2</sub>CO) and 1 (other line data). Table 1 lists the basic information about the resulting maps, including the frequency of the lines or continuum, the channel resolution (for line observations), the resulting synthesized beam and the *rms* noise of the maps.

## 3. Results

### 3.1. Dust continuum

The 1.35 mm continuum map shows that the emission is clearly resolved into two components, L723 SMA 1 and SMA 2, with similar intensities (see Figure 1) and separated by 2''.9 (880 AU in projected distance) with a position angle of 106°. These two components were previously detected by Launhardt (2004) at 3 mm. The strongest component, SMA 2, is associated with VLA 2A, 2B and 2C, 3.6 cm and 7 mm continuum sources that are probably young stellar objects (Carrasco-González et al. 2008). The other component, SMA 1, is only detected at 3 mm (Launhardt 2004) and marginally at 7 mm (source VLA 2D: Carrasco et al. 2008) and does not have known counterparts at other wavelengths. Table 2 gives the values of position, intensity, flux densities and the deconvolved sizes for both mm sources obtained by fitting a Gaussian to each component. The two sources are partially resolved at scales of about 1''.0–2''.0 (300–600 AU).

Naturally weighted maps were obtained in order to better estimate the total flux of the double core and to try to detect the WHS. The total flux density detected by our observations

---

<sup>1</sup>The Submillimeter Array is a joint project between the Smithsonian Astrophysical Observatory and the Academia Sinica Institute of Astronomy and Astrophysics, and is funded by the Smithsonian Institution and the Academia Sinica.

for SMA 2 and SMA 1 is  $128 \pm 6$  mJy, which is 22 mJy higher ( $\sim 20\%$ ) than that from the map shown in Figure 1, obtained with a robust weight of 0. This excess is possibly due to the better sensitivity of the natural weighted map to weak and extended emission. No emission is detected with the SMA at the position of WHS, with a  $3\text{-}\sigma$  upper limit of  $4.2 \text{ mJy beam}^{-1}$ . Gaussian tapers were applied to the visibilities to increase the beam size and see if the WHS could be detected, which yielded negative results.

The mass of the circumstellar material traced by the dust emission at mm wavelength, where it is optically thin is:

$$M = \frac{gS_\nu D^2}{\kappa_\nu B_\nu(T_{\text{dust}})} \quad (1)$$

with  $g$  the gas-to-dust ratio,  $D$  the distance,  $S_\nu$  the flux density,  $\kappa_\nu$  the dust mass opacity coefficient and  $B_\nu$  the Planck function for a blackbody of dust temperature  $T_{\text{dust}}$ . The major source of uncertainty in the mass derivation is the poor knowledge of the distance ( $300 \pm 150$  pc). To derive the mass we adopted  $g = 100$  (Draine 2004), a dust mass opacity of  $\kappa_{250\text{GHz}} = 0.9 \text{ cm}^2 \text{ g}^{-1}$  (Ossenkopf & Henning 1994). To estimate the temperature of the dust, we used the VLA  $\text{NH}_3$  (1,1) and (2,2) maps from Girart et al. (1997), which have a slightly higher angular resolution ( $3''.7 \times 3''.3$ ) than the SMA maps. Following the standard analysis procedure for these two ammonia lines, we obtain that at the SMA 1, SMA 2 and WHS peak positions the ammonia rotation temperature is  $\simeq 20$  K, which converted to the gas kinetic temperature of the gas is  $\sim 25$  K (Danby et al. 1988). Table 3 gives the mass derived for the different components using this value for the dust temperature. The total mass of the emission detected by the SMA is  $\sim 0.24 M_\odot$ , which is only a small fraction,  $\sim 5\%$ , of the dense envelope detected at larger scales (Girart et al. 1997; Shirley et al. 2002). WHS has a very small mass,  $\lesssim 0.01 M_\odot$ .

### 3.2. $\text{H}_2\text{CO}$

Figure 2 shows the channel maps for the  $\text{H}_2\text{CO}$   $3_{0,3}-2_{0,2}$  line. The  $\text{H}_2\text{CO}$  emission is concentrated around the two mm continuum sources, SMA 1 and SMA 2, although in most of the channels SMA 2 has brighter  $\text{H}_2\text{CO}$  emission than SMA 1. Toward SMA 2 the  $\text{H}_2\text{CO}$  emission peaks at or very close to the dust emission peak, whereas around SMA 1 the peak emission is, in some channels, displaced to the SE (only at  $v_{\text{LSR}} = 10.79 \text{ km s}^{-1}$  the  $\text{H}_2\text{CO}$  peaks at the same position as the dust). The kinematics of the two sources is difficult to disentangle because their separation is similar to the angular resolution. The first order moment of the emission shows velocity gradients along the two cores with velocity shifts up to  $\sim 1 \text{ km s}^{-1}$ . Although there is not a clear simple trend, the emission east of SMA 1 is clearly blueshifted with respect to the rest of the region. The velocity dispersion of the

H<sub>2</sub>CO emission (second-order moment map: see Fig. 4) changes little around the two cores, with values within the range of 0.5 to 0.7 km s<sup>-1</sup>, which corresponds, for a Gaussian line, to a full width at half maximum of 1.2 to 1.7 km s<sup>-1</sup>. This velocity dispersion range is larger than the one measured from VLA NH<sub>3</sub> observations,  $\leq 0.42$  km s<sup>-1</sup> (Girart et al. 1997). Figure 3 shows that the spectra of H<sub>2</sub>CO has larger line widths than those of NH<sub>3</sub> (note that the (1,1) and (2,2) transitions have hyperfine components, which broadens the line, specially for the (1,1)).

Since VLA 2 is a thermal radio jet with a well defined orientation (Anglada et al. 1996), position-velocity (PV) plots along ( $PA = 116^\circ$ ) and perpendicular ( $PA = 26^\circ$ ) to the radio jet orientation were made crossing VLA 2, which lies at the peak of SMA 2 (Figure 5). The PV plot along the radio jet direction passes very close to SMA 1 (see Fig. 5). In the direction perpendicular to the jet, the H<sub>2</sub>CO shows a velocity gradient ( $\sim 0.8$  km s<sup>-1</sup> within 1'' around VLA 2) that could be indicative of rotation. In the direction along the radio jet there is overlap of the emission between SMA 2 and SMA 1. Nevertheless, at the position of SMA 1 the H<sub>2</sub>CO emission shows a relative minimum. In Figure 5 we also show the PV plot centered on SMA 1 with a position angle of  $PA = 30^\circ$ , nearly perpendicular to the PV along the VLA 2 radio jet direction. This PV plot shows two weak peaks at different velocities,  $v_{\text{LSR}} \simeq 10.8$  and 11.9 km s<sup>-1</sup>, that are slightly shifted in position ( $\simeq 0''.9$ ).

As in the case of the continuum emission, no emission is detected at the position of the ammonia WHS (see Fig. 3). The 3- $\sigma$  upper limit from the SMA map is 0.53 Jy beam<sup>-1</sup> (2.4 K).

### 3.3. SiO

The SiO 5–4 line is marginally detected towards the SMA 1 and SMA 2 system (see Figure 6). The emission appears clumpy and elongated in the NW-SE direction ( $PA \simeq 145^\circ$ ), with the strongest emission about 11'' SE of SMA 1. Taking into account the fact that the SiO is a tracer of molecular shocks, the emission appears relatively “quiescent”: it is only slightly redshifted with respect to the systemic velocity (the emission is detected in the  $v_{\text{LSR}} = 11.31$  and 12.44 km s<sup>-1</sup> channels) and the line-width,  $\Delta v \simeq 2$  km s<sup>-1</sup>, is only slightly larger than that of the lines tracing the dense circumstellar material such as H<sub>2</sub>CO and ammonia.

The emission is apparently more associated with SMA 1, but given the complex outflow activity in the region (Lee et al. 2002; Carrasco-González et al. 2008) it is difficult to elucidate with which outflow and powering source it is associated. Nevertheless, at the SiO

velocity and location there is strong CO emission (see channel maps from Lee et al. 2002), which suggests that the SiO is tracing a region of interaction between the dense envelope and the outflow (Codella et al. 1999).

### 3.4. Other molecules

Several hyperfine transitions of the CN 2–1 rotational transition were detected (Fig. 8). The strongest line is a blend of three hyperfine lines, the  $F=7/2-5/2$ ,  $5/2-3/2$  and  $3/2-1/2$  of the  $J=5/2-3/2$  set. The  $J=3/2-5/2$ ,  $F=1/2-3/2$  hyperfine line is also marginally detected. Although there are other hyperfine transitions within the bandwidth their relative intensities were too small to be detected (see Fig. 8). The integrated intensity of the detected transitions (Fig. 7) shows that the emission is concentrated around VLA 2, being only weakly detected towards SMA 1. We also marginally detected the DCN 3–2 line toward the two sources (Figs. 7 and 8). Despite the poor spectral resolution ( $\sim 1 \text{ km s}^{-1}$ ), these two molecules show emission at the ambient molecular gas velocity with narrow line widths ( $\sim 1 \text{ km s}^{-1}$ ).

## 4. Analysis

### 4.1. Model of the dust emission

The dust emission from SMA 1 and SMA 2 are partially resolved with sizes of several hundred AU, which suggest that a significant contribution to the emission is possibly coming from the infalling envelopes around the disks. Figure 9 shows clearly that the correlated amplitude in the visibility data centered on VLA 2 comes mostly from an extended component, although there is also a weaker unresolved component, with a flux density of  $\sim 20 \text{ mJy}$ , that appears to be dominant at visibility radii larger than  $\sim 40 \text{ k}\lambda$ . To better characterize this apparently compact component, additional maps were obtained using only visibilities that have a radius in the  $(u, v)$  plane larger than  $45 \text{ k}\lambda$ . The resulting map of the emission from SMA 1 and SMA 2 appears to be compact. Both sources are unresolved with fluxes of  $19.7 \pm 2.4$  and  $13.3 \pm 2.4 \text{ mJy}$  for SMA 2 and SMA 1, respectively. This is about one third of the total flux density detected by the SMA for each source. A Gaussian fit to SMA 2 using the task IMFIT of AIPS yields an upper limit of the diameter of  $\simeq 1''.2$ : The other source, SMA 1, is too weak to do the same fitting. In any case, the compact dusty components seem to arise from a structure with a radius of  $\lesssim 180 \text{ AU}$ . Without proper modeling it is not possible to elucidate whether this compact component traces the disk or the inner part of the envelope. Interestingly, the peaks of the two components are slightly shifted ( $\sim 0''.4$ ) with respect to the peak

position given in Table 2. This could be produced by a somewhat asymmetrical distribution of the gas and dust in the envelope, which will not be a surprise because of the multiplicity detected with the VLA at the center of SMA 2. The compact component of SMA 2 coincides well with the centimeter source VLA 2A detected by Carrasco–González et al. (2008) (the position of the dust is  $\alpha(\text{J2000})= 19^{\text{h}}17^{\text{m}}53^{\text{s}}.666$  and  $\delta(\text{J2000})= 19^{\circ}12'19''.63$ ). The peak of the SMA 1 compact component ( $\alpha(\text{J2000})= 19^{\text{h}}17^{\text{m}}53^{\text{s}}.920$  and  $\delta(\text{J2000})= 19^{\circ}12'18''.52$ ) is displaced to the northwest with respect to VLA 2D by  $0''.67$  (see Fig. 10). Given the weak detection of this source at both 1.35 and 7 mm ( $5$  and  $4\text{-}\sigma$  respectively) further more sensitive observations are needed to confirm this displacement.

In order to characterize the properties of the double cores we modeled the dust emission assuming, for simplicity, that it arises from two independent optically–thin twin circumstellar envelopes with a radial density and temperature profiles at the position of the dusty sources detected with the SMA. The model integrates the dust emission assuming spherical symmetry from an inner radius,  $R_{\text{inner}}$ , to an outer radius of  $1.5 \times 10^4$  AU (this value is somewhat arbitrary and does not affect the fit because the emission at these scales is filtered out by the SMA). We do not include the possible contribution from the circumstellar disks, since it is possible that at this stage the disks are small, with a radius of  $\lesssim 30$  AU, (Rodríguez et al. 2005). The three possible protostars associated with SMA 2 are separated by a projected distance of  $\simeq 0''.9$  or 270 AU (Carrasco–González et al. 2008), below the angular resolution of our observations. If these sources are truly nearby protostars, it is possible that there is a cavity in the envelope between these sources. To check whether there is a significant cavity, we used different radii of 30, 100 and 180 AU. We adopted the density profile expected for an infalling envelope,  $n(r) \propto r^{-1.5}$ , up to an infall radius,  $R_{\text{infall}}$ . Beyond  $R_{\text{infall}}$  we used a  $r^{-2}$  density profile. In order to minimize the free parameters in the model, we adopted a  $R_{\text{infall}} = 1000$  AU, the value found by Shirley et al. (2002). For a dusty cloud heated by an internal source, the temperature radial profile can be characterized as  $T \propto r^{-2/(4+\beta)}$  (Kenyon et al. 1993), where  $\beta$  is the dust emissivity spectral index. The value used is  $\beta = 1.5$ , which was derived from 850 and 450  $\mu\text{m}$  SCUBA observations (Estalella et al. 2003). We adopted an 1.35 mm dust opacity of  $\kappa \simeq 0.9 \text{ cm}^2$ , which should be adequate for dusty particles with ice mantles at densities of about  $10^6 \text{ cm}^{-3}$  according to Ossenkopf & Henning (1994). Additional free parameters were the density  $n_0$  and temperature  $T_0$  at a radius of 1,000 AU. Intensity profiles were obtained for each set of  $R_{\text{inner}}$ ,  $n_0$  and  $T_0$  and converted to a 2-D image map. These modeled maps were multiplied by the primary beam response of the SMA antennae, assumed to be  $56''$  at 1.35 mm. Two sets of visibility data were generated: one obtained by subtracting the modeled map to the visibility continuum data of the SMA observations. The other set was obtained by replacing the values of observed visibilities with the values expected from the modeled map. Maps of the residual and of the



model were obtained from the visibilities using the same parameters as the SMA maps shown here. The *rms* and *bias* was finally computed for these residual maps. The bias is defined as the absolute flux density of the residual on a given region (the region where the emission is detected). The models with an inner radius of 180 AU cannot reproduce well the SMA data, which suggests that if there is an inner cavity (produced by the presence of a multiple protostellar system), it is not big enough to affect the simple model used here. With respect to the solutions with an inner radius of 30 and 100 AU, there is, for both, a family of possible solutions in the  $T_0$ – $n_0$  plane. The plot of the *rms* for these two inner radii in the range of densities and temperatures computed are shown in Figure 11. The best set of solutions can be expressed as  $n_0 = 1.5 \times 10^6 [T_0/30 \text{ K}]^{-1.2} \text{ cm}^{-3}$  and  $1.1 \times 10^6 [T_0/30 \text{ K}]^{-1.2} \text{ cm}^{-3}$  for the 30 and 100 AU inner radius, respectively.

The VLA ammonia maps from Girart et al. (1997) can be used to further constrain the model. At the positions of SMA 1 and SMA 2 the kinetic temperature estimated from the  $\text{NH}_3$  (1,1) and (2,2) maps is  $\simeq 25$  K (see § 3.1). Since the beam of the VLA maps is  $\simeq 3''.5$ , it is reasonable to adopt the value of  $1''.75$  or 520 AU, as the radius at which the gas is at 25 K. This implies that the temperature profile of the dust can be written as  $T = 20 (r/1000 \text{ AU})^{-0.35}$  K. The previous two equations that give the best set of solutions yield a density profile of  $n(\text{H}_2) = 2.4 \times 10^6 (r/1000 \text{ AU})^{-1.5} \text{ cm}^{-3}$  for  $R_{\text{inner}} = 30$  AU, and of  $1.8 \times 10^6 (r/1000 \text{ AU})^{-1.5} \text{ cm}^{-3}$  for  $R_{\text{inner}} = 100$  AU. Figure 9 shows that the correlated flux in the visibility domain for the model with  $R_{\text{inner}} = 30$  AU,  $T_0 = 20$  K and  $n_0 = 2.4 \times 10^6 \text{ cm}^{-3}$  fits reasonably well the SMA data. The synthetic maps from the model and from the residuals for this particular solution also show the remarkable similitude with the L723 dusty binary system (see Fig. 12). Indeed, from the residual map obtained using only the longest baselines (see right panels of Fig. 12) the model of the binary envelope can account within the *rms* level of the map the compact, apparently unresolved, component of the two dusty sources, without the need of invoking the presence of an accretion disk (see the discussion section). On the other hand, the residual map done using all the visibilities shows some significant residuals (at a  $\sim 4\text{-}\sigma$  level): there are some positive residuals northeast of SMA 2 and extended negatives on the southern side of the dust emission from both SMA 1 and SMA 2. These residuals could be due to the departure from the spherical symmetry of the data.

We can also compare the density we found with the value derived by Dartois et al. (2005) by modeling the spectral energy distribution of L723. They estimated that at 100 AU the density is  $2.2 \times 10^7 \text{ cm}^{-3}$ , which is a factor 2.6 to 3.4 lower than what we derive for  $T_0 = 20$  K. This difference could be due to the different dust opacity and the different density profile used.

The derived density distribution can be used to estimate the mass of the two envelopes.

The equivalent radius of the SMA shortest baselines in the visibility domain ( $\simeq 12 \text{ k}\lambda$ ) is  $3''.75$  (1125 AU). The combined mass for the two envelope within a radius of 1125 AU is in the 0.14–0.36  $M_{\odot}$  range for a temperature range of  $T_0 = 20\text{--}30 \text{ K}$  and of  $R_{\text{inner}} = 30\text{--}100 \text{ AU}$ . These values are compatible with the mass estimated in Table 3.

As an additional test for the model, we have used a 3.2 mm continuum map obtained with the BIMA array. These observations were carried out in September 2003 in the C configuration. The continuum was observed simultaneously with the  $\text{N}_2\text{H}^+$  1–0 and  $\text{CH}_3\text{OH}$   $2_{0-1_0}$  A and  $2_{-1-1_{-1}}$  E lines (Masqué, Girart & Estalella, in preparation). The dust model was extrapolated to this wavelength, and the standard position of the BIMA antennas at the C configuration were used to create a synthetic BIMA map using the same procedure as the one described for the SMA. The synthetic maps were obtained for the  $R_{\text{inner}} = 30 \text{ AU}$ ,  $T_0 = 20 \text{ K}$  and  $n_0 = 2.4 \times 10^6 \text{ cm}^{-3}$  model. Figure 13 shows that the model also reproduces reasonably well the BIMA map.

#### 4.2. Modeling the $\text{H}_2\text{CO}$ emission

Once the dust emission was successfully modeled, we modeled the  $\text{H}_2\text{CO}$  emission using the one dimensional version of Ratran (Hogerheijde & van der Tak 2000). This is a Monte Carlo code that calculates the radiative transfer and excitation of molecular lines. The code is formulated from the viewpoint of cells rather than photons, which allows the separation of local and external contributions of the radiation field. This gives an accurate and fast performance even for high opacities (Hogerheijde & van der Tak 2000). The  $\text{H}_2\text{CO}$  collisional rates used were derived by Green (1991) and were downloaded from the Leiden Atomic and Molecular Database (Schöier et al. 2005).

We modeled the emission as arising from two cores with the same density and temperature profile, as suggested by the dust modeling. Since there is a family of possible solutions, we fixed the temperature and density profiles derived in the previous section that agrees with the ammonia rotational temperature:  $T = 20 (r/1000 \text{ AU})^{-0.35} \text{ K}$  and  $n(\text{H}_2) = 2.4 \times 10^6 (r/1000 \text{ AU})^{-1.5} \text{ cm}^{-3}$  (the solution for  $R_{\text{infall}} = 30 \text{ AU}$ ).

The kinematics is not well resolved with our observations, so we assume that the gas is in free-fall collapse. This is marginally suggested by the line profile at the position of SMA 1 and SMA 2 (see Fig. 14 and § 5.1). We adopted a velocity field for the free-falling gas of  $v_{\text{infall}} = 0.5 (r/1000 \text{ AU})^{-0.5} \text{ km s}^{-1}$  and an intrinsic linewidth of  $0.6 \text{ km s}^{-1}$ . Using these values the modeled line width was similar to the  $\text{H}_2\text{CO}$  values measured with the SMA and, in any case, the use of these values should not affect critically the derivation of the  $\text{H}_2\text{CO}$

properties (Jørgensen et al. 2004).

To run RATRAN we adopted a fixed H<sub>2</sub>CO abundance within a shell with an inner and outer radius  $R_{in}$  and  $R_{out}$ , respectively, with the abundance being zero outside the shell. We ran a series of models with Ratran using a range of values for  $R_{in}$  and  $R_{out}$  and for the p-H<sub>2</sub>CO abundance,  $X[\text{p-H}_2\text{CO}]$ . Since the H<sub>2</sub>CO emission is significantly different between the two envelopes, we made synthesized maps using different sets of  $(R_{in}, R_{out}, X[\text{p-H}_2\text{CO}])$  values for SMA 1 and SMA 2. Synthesized maps with 16 channels and with a spectral resolution of 0.28 km s<sup>-1</sup> were generated. We took into account that the systemic velocity of the H<sub>2</sub>CO between the two cores differs by  $\simeq 0.2$  km s<sup>-1</sup> (see Table 4). The maps were multiplied by the primary beam of the SMA and then converted to visibilities. Maps of the model and of the residuals (generated by subtracting the model to the data in the visibility domain) were made in the same fashion as for the SMA dust emission maps (see § 4.1).

We explored values within the range of  $8 \times 10^{-11}$  to  $1 \times 10^{-8}$  for  $X[\text{p-H}_2\text{CO}]$ , 30 to 240 AU for  $R_{in}$  and 300 to  $10^4$  AU for  $R_{out}$ . In order to find the best set of solutions, we computed separately the  $\chi^2$  parameter for the spectra at the SMA 1 and SMA 2 positions and for the total flux density within a region of  $11'' \times 8''$  centered around the twin envelopes. Table 5 shows the range of the best fits found. The range of parameters is better constrained for SMA 2 than for SMA 1. This is due to its higher intensity and its apparently more compact size. Indeed, the model yields solutions that imply that the H<sub>2</sub>CO around SMA 2 should arise from the inner region of the envelope. More specifically, the outer radius cannot be significantly larger than 600 AU, but not lower than 300 AU (otherwise the emission would be unresolved, which is not the case). The SMA 2 abundance is also relatively well constrained,  $X[\text{p-H}_2\text{CO}] \simeq (3-10) \times 10^{-10}$ . For SMA 1, the best set of solution yields H<sub>2</sub>CO abundances in the range  $X[\text{p-H}_2\text{CO}] \simeq (8-30) \times 10^{-11}$ , but with values always lower than for SMA 2: the best solutions are found when SMA 2 abundances are a factor of 3 to 10 higher than for SMA 1. Another difference with respect to SMA 2 is that the best models for SMA 1 have a larger outer radius than for SMA 2,  $R_{out} \simeq 600-5000$  AU.

Figure 15 shows the synthesized model, the SMA data and the residual for one of the best solutions found (see the figure caption for details). Figure 14 shows the spectra toward SMA 1 and SMA 2 for the same model and for the SMA data. These figures show that the models fit the observations reasonably well, although the residuals appear up to about a  $4\text{-}\sigma$  level. In spite of the good match between the synthesized and observed spectra for the two sources, the model reproduces better the morphology of SMA 2 than that of SMA 1. The morphology mismatch between SMA 1 and the synthesized map occurs for all the models. This suggest that the emission, specially from SMA 1, departs from the idealized spherical model used with the assumption that the H<sub>2</sub>CO arises only within a shell. Indeed, the

position–velocity cuts in two orthogonal directions centered on SMA 1 (see Fig. 5) show a double peak in one of them and what roughly appear to partially be a “donut”, centered on SMA 1, in the other cut (partially because of the overlap with SMA 2 in the NW side). This suggests that the H<sub>2</sub>CO emission may not come from the shell of a spherical envelope but from a contracting and somewhat flattened shell or torus. For example, such a case was more clearly observed in the CS emission associated with the dense core ahead of HH 80N (Girart et al. 2001). The marginal evidence that the H<sub>2</sub>CO arises from a torus supports the idea that the emission does not come from a spherical configuration. However, despite the limitations of the adopted approach, given the limited signal-to-noise ratio obtained and the use of only one transition, the results from the modeling should be regarded as a good first approximation to the properties of H<sub>2</sub>CO in these two cores.

The derived p–H<sub>2</sub>CO abundances are compatible with the value found by Jørgensen et al. (2005),  $9.6 \times 10^{-10}$ , from single-dish observations, and are also within the range of values found for the so-called outer part of the circumstellar envelopes associated with Class 0 sources (Jørgensen et al. 2005; Maret et al. 2004), which are defined as the region where temperatures are lower than  $\simeq 100$  K. In the inner region of the envelopes, where the temperature is  $\gtrsim 100$  K, the icy grain mantles evaporates and molecular abundances are expected to increase significantly: the H<sub>2</sub>CO reaches abundances between  $10^{-8}$  and  $10^{-6}$  (Jørgensen et al. 2005; Maret et al. 2004). Our model did not take into account this warm component. Nevertheless, the reasonable solutions found in this paper imply that the total amount of H<sub>2</sub>CO in the inner warm region is not significant, despite the very high H<sub>2</sub>CO abundance expected. This can be explained by the fact that for L723, the warm region is very small due to its low total bolometric luminosity,  $3.4 L_{\odot}$  (the temperature of 100 K is reached at a radius of 10 AU).

## 5. Discussion

### 5.1. The Twin Cores

The dust emission reveals two similar substructures, with SMA 2 being only slightly more massive than SMA 1 (Table 2). In fact, the modeling of the emission suggest that within the observational uncertainties (sensitivity and angular resolution) the dust properties of the two cores can be accounted as arising from “identical” twin cores. However, these twin cores have different molecular properties. The CN 2–1 and H<sub>2</sub>CO 3<sub>03</sub>–2<sub>02</sub> emission is stronger in SMA 2 than in SMA 1. In fact, the modeling carried out in § 4.2 shows that the H<sub>2</sub>CO associated with SMA 2 has a higher molecular abundance (by a factor 3–10) and arises from a more compact region than in SMA 1. In both cores, the line width of the H<sub>2</sub>CO

lines are clearly larger (by up to 50%) than those of  $\text{NH}_3$ . In addition, the  $\text{H}_2\text{CO}$   $3_{03}-2_{02}$  emission is more compact than the  $\text{NH}_3$  emission, as can be clearly seen in Fig. 7. These two features taken together are a good indication of the presence of radial velocity gradients, with increasing velocity with decreasing radius to protostars. Both infall and rotation velocities are expected to have this behavior. The presence of a blueshifted peak slightly higher than the redshifted one at the position of the two cores (Fig. 14) is an additional marginal evidence of infall motions.

Previous observations find clear star formation signatures associated with the SMA 2 core. First the presence of a well studied thermal radio jet, VLA 2A, pinpoint the position of a protostar that is powering the east–west molecular outflow (Anglada et al. 1996; Carrasco–González et al. 2008). VLA high angular resolution observations reveal the presence of a water maser, and 7 mm and 3.6 cm sources (VLA 2B and 2C)  $\sim 0''.5$  around VLA 2A (Girart et al. 1997; Carrasco–González et al. 2008). Carrasco–González et al. (2008) interpret these as a young stellar system, which is forming in the 150 AU vicinity (in projected distance) around VLA 2A. In addition, they find that VLA 2B may be powering the north–south molecular outflow. This stellar system is being formed inside the SMA 2 core. In contrast, there are not known signs of outflow activity towards SMA 1, yet. There is only marginal dust emission detected at 7 mm, labeled as VLA 2D (Carrasco–González et al. 2008).

In conclusion, our study and analysis of SMA 1 and SMA 2 show that they have almost identical properties (mass, and density and temperature distribution) and that there is marginal evidence of infall motions in both. However, the  $\text{H}_2\text{CO}$  abundance towards SMA 2 is significantly higher than in SMA 1. Since SMA 2 shows clear outflow activity, in contrast with SMA 1, this suggests that SMA 2 is more evolved (due to a higher infall rate or because it is older). In any case, they are not “identical” twin cores but “fraternal” twin cores.

## 5.2. The Mass Reservoir around the Class 0 protostellar system

The total mass derived from the SMA observations is less than 10% of the whole dense core, derived from SCUBA JCMT observations at 850 and 450  $\mu\text{m}$  (Estalella et al. 2003) or from VLA  $\text{NH}_3$  observations (Girart et al. 1997). That is, the mass accreting to the protostars (or to the disks) at scales of  $\lesssim 1000$  AU is only a small part of the dense core. In addition, from the modeling we found that the dust emission detected by the SMA at 1.35 mm seems to arise from the dense twin envelopes, SMA 1 and SMA 2, and within the limits of our sensitivity there is no need to invoke to the presence of protostellar disks. That means that the contribution from the disks at 1.35 mm should not be higher than  $\simeq 8$  mJy

(the  $5\text{-}\sigma$  value of the continuum residual map of Fig. 12). Assuming that the disk has a temperature of 50 K, the upper limit of the disk mass is  $6 \times 10^{-3} M_{\odot}$ . This mass would be higher if the dust emission from the disk is not optically thin, but it would be lower if the temperature is higher. In any case, this suggests that the disk mass is less than 10% of the mass of each of the twin cores. Thus, the large scale (0.1 pc) molecular envelope traced by  $\text{NH}_3$  or SCUBA contain most of the mass or, in other words, it is still the major reservoir of mass to keep the star formation going on. Therefore, L723 seems to be in a very early phase of star formation.

It is clear that fragmentation is occurring at different levels. The 0.1 pc scale molecular envelope has fragmented at the center and at scales of  $\simeq 1000$  AU into two cores, SMA 1 and SMA 2. At the same time, at least one of these cores, SMA 2, has undergone additional fragmentation at scales of  $\simeq 150$  AU, forming a multiple stellar system. However, we note that within the uncertainties, the SMA 2 can be modeled a single envelope down to a radius of 30 AU. It is interesting to note that whatever is the fragmentation process that is acting in the different scales (turbulence, the initial magnetic field and angular momentum configuration) is occurring within a 0.1 pc dense envelope that appears to be very quiescent at scales of few thousands AU outside its center according to the  $\text{NH}_3$  data (Girart et al. 1997): line widths of only  $\lesssim 0.5 \text{ km s}^{-1}$  and small velocity gradients, of  $3 \text{ km s}^{-1} \text{ pc}^{-1}$ .

## 6. Summary

We present continuum and line 1.35 mm high angular resolution observations ( $\simeq 3''$ ) carried out with the SMA toward the low-mass protostellar region in the L723 dark cloud. We detected emission of the dust, the  $\text{H}_2\text{CO } 3_{0,3}\text{-}2_{0,2}$ , DCN 3–2 and SiO 5–4 transitions, as well as a few lines of the CN 2–1 transition. We performed a radiative transfer analysis of the dust emission as well as for the  $\text{H}_2\text{CO}$  line in order to constrain the physical and chemical conditions of the two cores. The main results of the paper can be summarized as:

1. The dust emission arises from two similar cores, SMA 1 and SMA 2, separated by  $2''.9$  (880 AU in projected distance) and with masses of 0.06 and 0.08  $M_{\odot}$ , respectively. They are partially resolved, with deconvolved sizes of  $\sim 500$  AU. SMA 2 is associated with VLA 2 and water maser emission. We modeled the dust emission from the two cores assuming that the cores have a density and temperature radial distribution of the type:  $n(r) \propto r^{-1.5}$  and  $T \propto r^{-0.35}$ . We found that within the uncertainty achieved, the two cores can be considered almost “identical” twins. The best set of solutions are those with a density and temperature that match the following expression:  $n_0(\text{H}_2) = 1.45 \times 10^6 [T_0/30 \text{ K}]^{1.2} \text{ cm}^{-3}$  ( $n_0$  and  $T_0$  are the density and temperature at a radius

of 1000 AU). The model shows that all the emission detected can arise from the cores, with possibly no evidence of contribution from the accretion disk, which yields an upper limit of the disk mass of  $\sim 6 \times 10^{-3} M_{\odot}$ .

2. The H<sub>2</sub>CO emission is concentrated around the two mm continuum sources, SMA 1 and SMA 2, although the emission is brighter toward SMA 2. The kinematics of the two sources is difficult to disentangle because their separation is similar to the angular resolution. Nevertheless, there is marginal evidence of infall motions in both sources (double peak line, with brighter blueshifted component), of a velocity gradient around SMA 2 indicative of rotation, and that the H<sub>2</sub>CO in SMA 1 arises from a contracting and somewhat flattened structure. The linewidth of H<sub>2</sub>CO has values in the 1.2–1.7 km s<sup>−1</sup> range, which is  $\sim 50\%$  larger than the values measured for the NH<sub>3</sub> lines by Girart et al. (1997). The H<sub>2</sub>CO emission was modeled adopting the density and temperature profile constrained by the dust emission. We used RATRAN assuming a fixed p–H<sub>2</sub>CO abundance within a shell with an inner and outer radius  $R_{in}$  and  $R_{out}$ , respectively, being the abundance zero outside the shell. Reasonable models were found for a p–H<sub>2</sub>CO abundance range of  $(3–10) \times 10^{-10}$  and  $(8–30) \times 10^{-11}$  for SMA 2 and SMA 1, respectively, but with the SMA 1 abundance lower than for SMA 2 by a factor 3 to 10. The best models are those that have a more compact emission in SMA 2 ( $R_{out} \simeq 300–600$  AU) than in SMA 1 ( $R_{out} \simeq 600–5000$  AU). The p–H<sub>2</sub>CO abundances found are compatible with the value of the outer part of the circumstellar envelopes associated with Class 0 sources. The total amount of H<sub>2</sub>CO in the inner warm region of the circumstellar envelopes (where  $T \gtrsim 100$  K) is not significant, despite the very high H<sub>2</sub>CO abundance expected (e.g.; Maret et al. 2004). This can be explained by the fact that for L723, the warm region is very small (a radius of  $\lesssim 10$  AU) due to its low total bolometric luminosity,  $3.4 L_{\odot}$ .
3. The DCN and CN lines arise from the same region than the dust and H<sub>2</sub>CO. The CN emission peaks clearly toward SMA 2, whereas the DCN shows similar emission in SMA 1 and in SMA 2.
4. SiO is detected marginally at slightly redshifted velocities around SMA 1 and SMA 2, and is possibly tracing a region of interaction between the dense envelope and the outflow.
5. The Western Hot Spot (WHS), detected by Girart et al. (1997) from NH<sub>3</sub> observations as a spot of local heating, is not detected by the SMA (line and continuum) observations. The non-detection of the 1.35 mm emission yields an upper limit of the WHS mass of  $\simeq 0.01 M_{\odot}$ .

6. The above results suggest that although SMA 1 and SMA 2 cores have almost identical physical properties (density and temperature distribution), they are rather “fraternal” twin cores, with SMA 2 being in a more evolved stage. Thus, SMA 2 is harboring an active multiple low-mass protostellar system (VLA 2A, 2B and 2C), powering at least one molecular outflow (Carrasco-González et al. 2008). In contrast, there are not signs of outflow activity towards SMA 1.
7. The large scale, 0.1 pc, molecular envelope (traced by  $\text{NH}_3$  or SCUBA) is the major reservoir of mass to keep the star formation going on (it contains about  $\gtrsim 90\%$  of the mass), which suggests that L723 is still in a very early phase of star formation.
8. Fragmentation is occurring at different levels at the center of the L723 dense molecular cloud: at scales of  $\simeq 1000$  AU the cloud has fragmented into two cores, SMA 1 and SMA 2, and SMA 2 has undergone additional fragmentation at scales of  $\simeq 150$  AU, forming a multiple stellar system (Carrasco-González et al. 2008). Whatever is the fragmentation process that is acting at the different scales (turbulence, the initial magnetic field and angular momentum configuration) it is occurring within a 0.1 pc dense envelope that appears to be at larger scales.

JMG is grateful to the SMA staff at Hilo for the support during the visit to the SMA. We would like to thank the anonymous referee for the valuable comments. JMG acknowledges support from the DURSI (Generalitat de Catalunya) grant BE-2004-00370. JMG and RE are supported by MICINN grant AYA2005-05823-C03 (co-funded with FEDER funds).

## REFERENCES

- André, P., Ward-Thomson, D., & Barsony, M. 1993, *ApJ*, 406, 122
- Anglada, G. 2004, *Revista Mexicana de Astronomia y Astrofisica Conference Series*, 21, 100
- Anglada, G., Estalella, R., Rodríguez, L.F., Torrelles, J.M., Lopez, R., & Cantó, J. 1991, *ApJ*, 376, 615
- Anglada, G., Rodríguez, L. F., & Torrelles, J. M. 1996, *ApJ*, 473, L123
- Avery, L.W., Hayashi, S.S., & White, G.J. 1990, *ApJ*, 357, 524
- Carrasco-González, C., Anglada, G., Rodríguez, L. F., Torrelles, J. M., Osorio, M., & Girart, J. M. 2008, *The Astrophysical Journal*, 676, 1073



- Chen, X., Launhardt, R., & Henning, T. 2007, *ApJ*, 669, 1058
- Codella, C., Bachiller, R., & Reipurth, B. 1999, *A&A*, 343, 585
- Danby, G., Flower, D. R., Valiron, P., Schilke, P., & Walmsley, C. M. 1988, *MNRAS*, 235, 229
- Davidson, J.A. 1987, *ApJ*, 315, 602
- Dartois, E., Pontoppidan, K, Thi, W.-F., & Muñoz Caro, G. M. 2005, *A&A*, 444, 57
- Draine, B. T. 2004, *The Cold Universe*, Saas-Fee Advanced Course 32, Springer-Verlag, Lecture Notes 2002 of the Swiss Society for Astronomy and Astrophysics (SSAA), Springer, 2004. Edited by A.W. Blain, F. Combes, B.T. Draine, D. Pfenniger and Y. Revaz, p. 213
- Estalella, R., Palau, A., Girart, J.M., Beltran, M.T., Anglada, G. Ho, P.T.P., & Osorio, M. 2003, *Revista Mexicana de Astronomia y Astrofisica Conference Series*, 15, 135
- Furuya, R. S., Kitamura, Y., Wootten, A., Claussen, M. J., & Kawabe, R. 2003, *ApJS*, 144, 71
- Girart, J.M., Estalella, R., Anglada, G., Torrelles, J.M., Ho, P.T.P., & Rodriguez, L.F. 1997, *ApJ*, 489, 743
- Girart, J. M., Estalella, R., Viti, S., Williams, D. A., & Ho, P. T. P. 2001, *ApJ*, 562, L91
- Goldsmith, P.F., Snell, R.L., & Hemeon-Heyer, M. 1984, *ApJ*, 286, 599
- Green, S. 1991, *ApJS*, 76, 979
- Hayashi, S.S., Hasenawa, T., & Kaifu, N. 1991, *ApJ*, 377, 492
- Hirano, N., Hayashi, S. S., Umemoto, T., & Ukita, N. 1998, *ApJ*, 504, 334
- Hogerheijde, M. R., & van der Tak, F. F. S. 2000, *A&A*, 362, 697
- Jørgensen, J. K., Schöier, F. L., & van Dishoeck, E. F. 2004, *A&A*, 416, 603
- Jørgensen, J. K., Schöier, F. L., & van Dishoeck, E. F. 2005, *A&A*, 437, 177
- Kenyon, S. J., Calvet, N., & Hartmann, L. 1993, *ApJ*, 414, 676
- Launhardt, R. 2004, *IAU Symp.* 221, 213

- Lee, C.-F., Mundy, L.G., Stone, J.M., & Ostriker, E. C. 2002, *ApJ*, 576, 294
- López, R., Estalella, R., Gómez, G., & Riera, A. 2007, *A&A*, 454, 233
- Maret, S., et al. 2004, *A&A*, 416, 577
- Moriarty-Schieven, G.H.,& Snell, R.L. 1989, *ApJ*, 338, 952
- Ossenkopf, V., & Henning, T. 1994, *A&A*, 291, 943
- Palacios, J.,& Eiroa, C. 1999, *A&A*, 346, 233
- Pezzuto, S., Grillo, F., Benettini, M., et al. 2002, *MNRAS*, 330, 1034
- Rodríguez, L. F., Loinard, L., D’Alessio, P., Wilner, D. J., & Ho, P. T. P. 2005, *ApJ*, 621, L133
- Shirley, Y., Evans N.J., & Rawlings, J. 2002, *ApJ*, 575, 337
- Schöier, F. L., van der Tak, F. F. S., van Dishoeck E. F., & Black, J. H. 2005, *A&A*, 432, 369

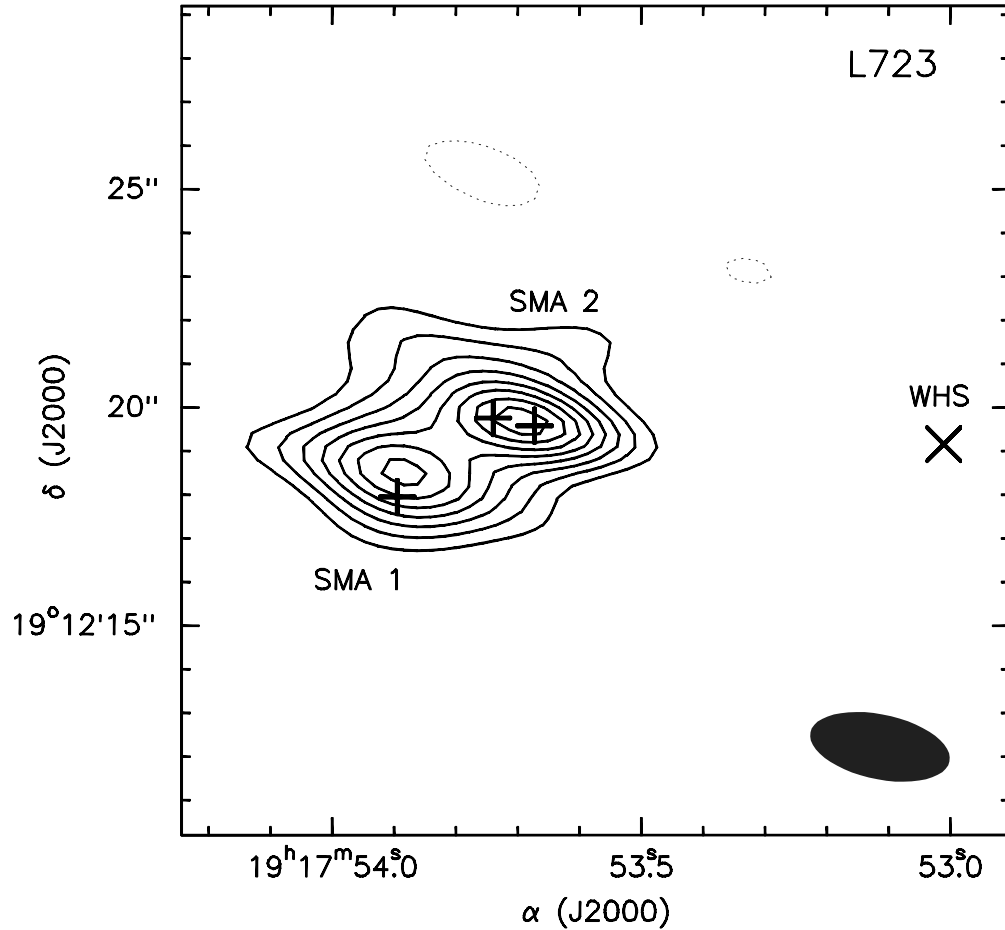


Fig. 1.— SMA map of the continuum emission at 1.35 mm (222.31 GHz) toward L723 VLA 2. Contour levels are  $-3, 3, 5, 7, 9, 11, 13, 15$  and  $17$  times  $1.8 \text{ mJy beam}^{-1}$ , the rms noise of the map. The synthesized beam is shown in the lower right corner. The crosses show the position of VLA 2A (the western cross) and VLA 2C, which are associated with SMA 2, and VLA 2D, associated with SMA 1. These sources were detected by the VLA at 3.6 and 7 mm from sub-arcsecond maps by Carrasco-González et al. (2008). The titled cross shows the position of the WHS (Girart et al. 1997).

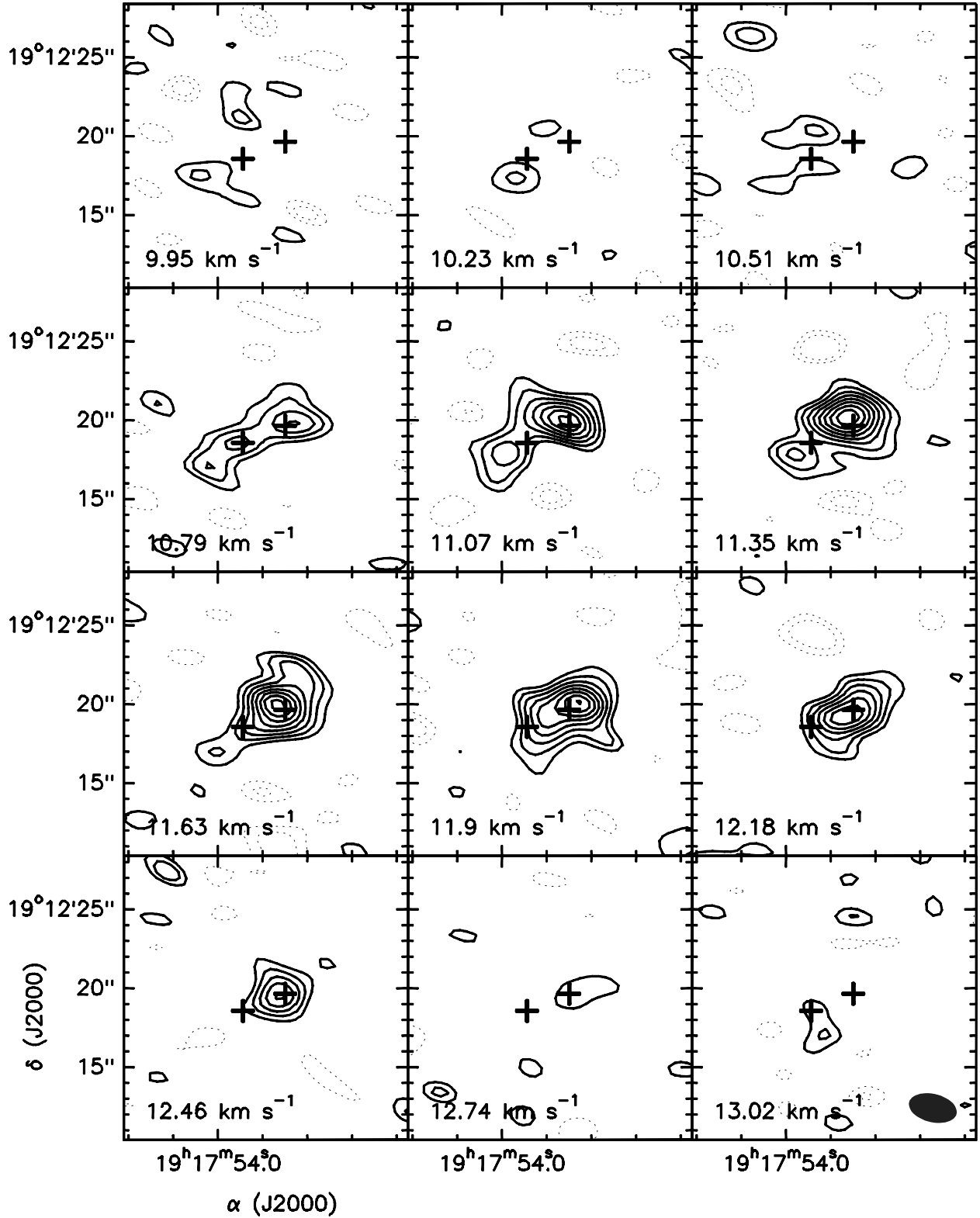


Fig. 2.— SMA map of the H<sub>2</sub>CO 3<sub>0,3</sub>-2<sub>0,2</sub> emission toward L723 VLA 2. Contour levels are -2, 3, 4, 5, 6, 7 and 8 times 0.18 Jy beam<sup>-1</sup>, the rms noise of the map. The synthesized beam is shown in the lower right corner of the lower right panel. The crosses show the position of the dust sources SMA 1 and SMA 2. The  $v_{\text{LSR}}$  velocity of the channels is shown in the lower left corner of the panels.

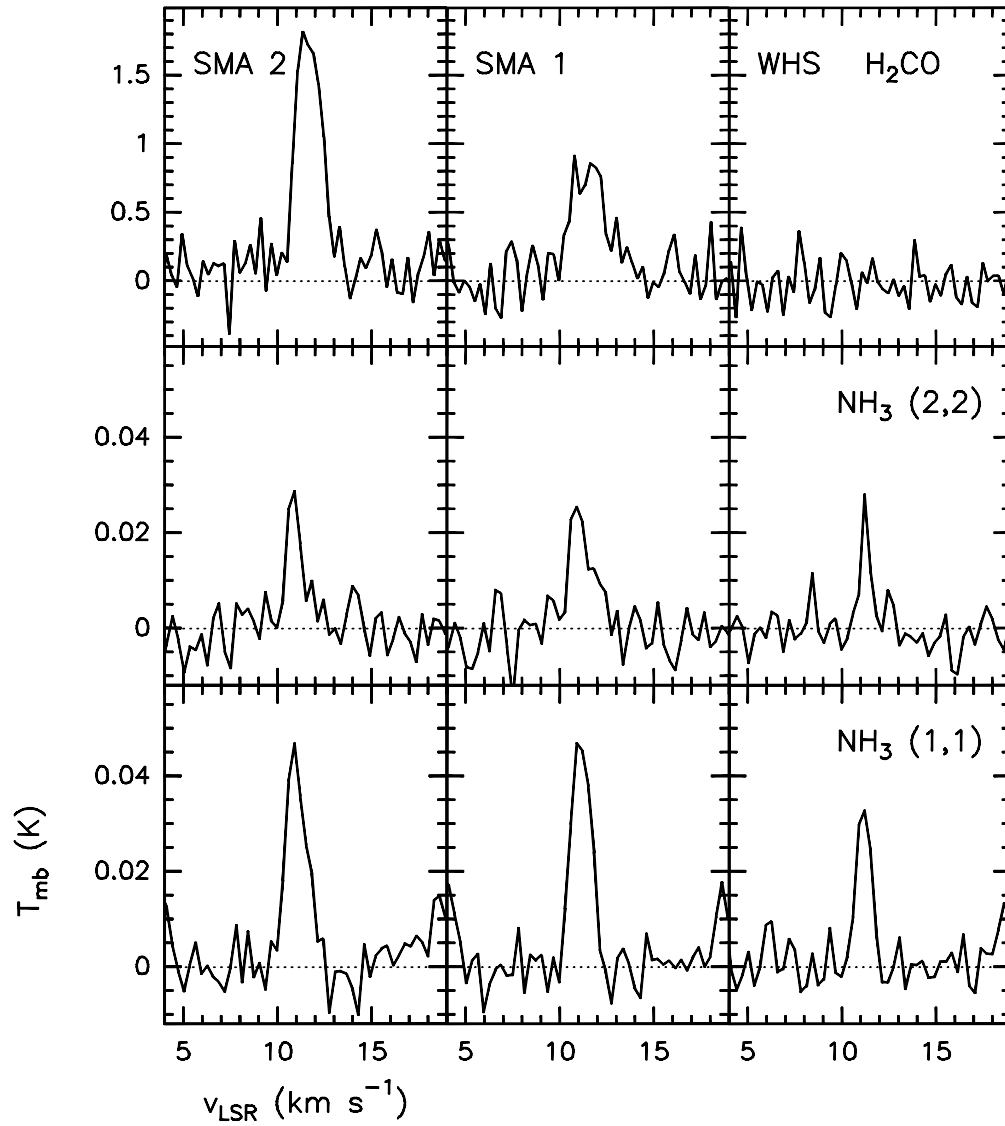


Fig. 3.— Spectra of the H<sub>2</sub>CO  $3_{0,3}-2_{0,2}$ , NH<sub>3</sub> (2,2) and (1,1) toward the position of SMA 2 (left panels), SMA 1 (central panels) and WHS (right panels). The spectra were taken from channel maps at similar angular resolution,  $\sim 3''$ . The NH<sub>3</sub> spectra are taken from Girart et al. (1997).

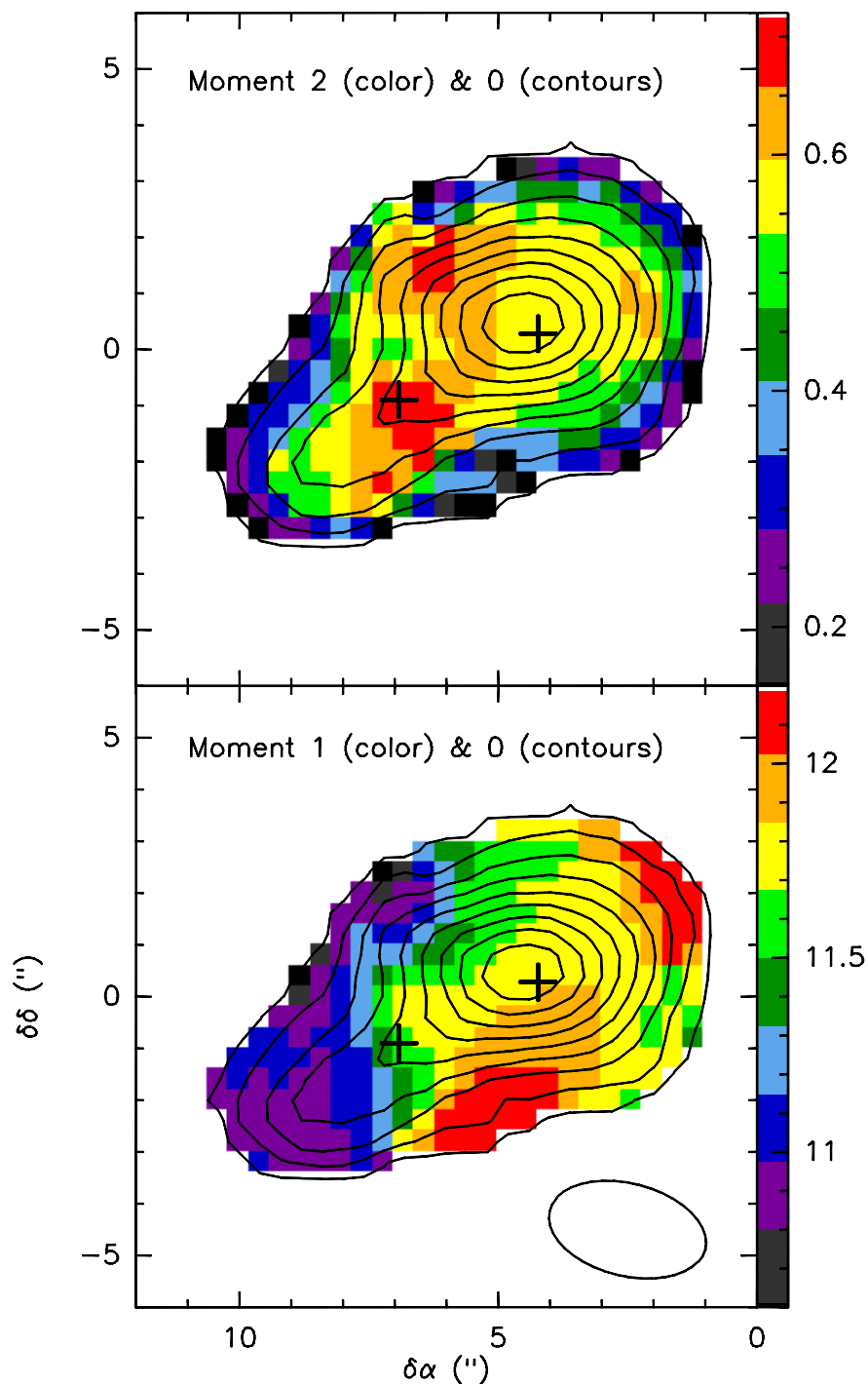


Fig. 4.— Color image of the first order (bottom panel) and second order (top panel) moments of the  $\text{H}_2\text{CO}$  emission towards L723 VLA 2 superposed with the zero order moment (integrated emission) contour map. The color image level is shown in the right side of the panels. The first contour is  $0.1 \text{ Jy beam}^{-1} \text{ km s}^{-1}$ , and the contour levels are  $0.3 \text{ Jy beam}^{-1} \text{ km s}^{-1}$ . The crosses show the position of the dust sources SMA 1 and SMA 2. The synthesized beam of the maps is shown in the bottom right corner of the bottom panel.

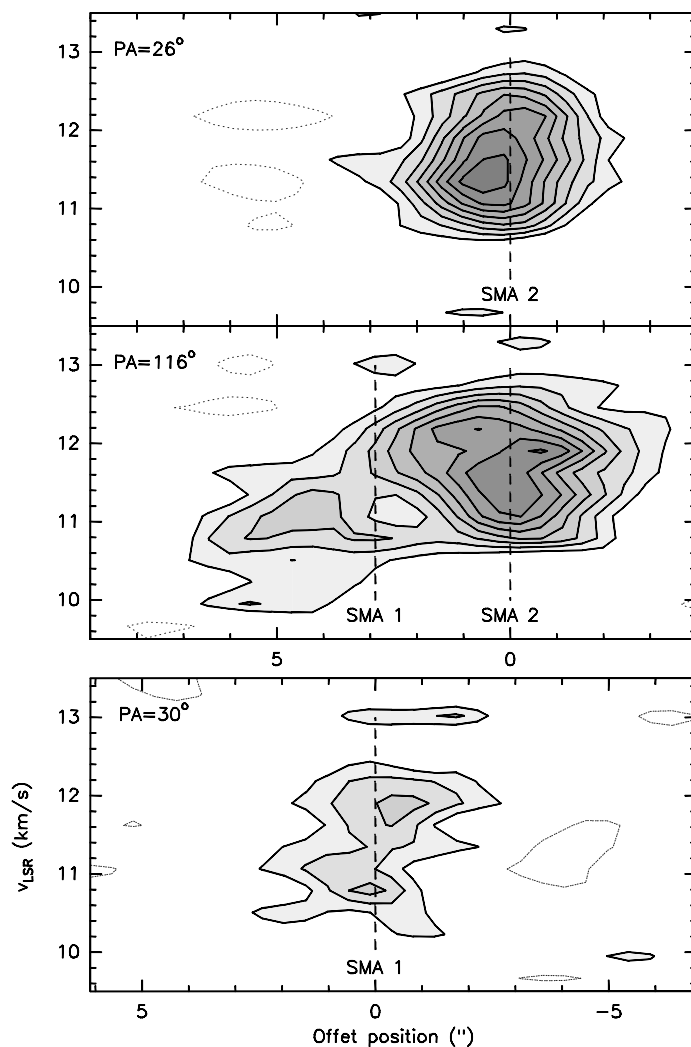


Fig. 5.— Position-velocity (PV) plots of the  $\text{H}_2\text{CO } 3_{0,3}-2_{0,2}$  emission. The *top* and *central* panels show the PV plot perpendicular and along the VLA 2 thermal radio jet direction,  $PA = 26^\circ$  and  $116^\circ$ , respectively, centered on SMA 2 (and VLA 2). The *bottom* panel shows the PV plot centered on SMA 1 with a position angle,  $PA = 30^\circ$  nearly perpendicular to the VLA 2 radio jet and similar to the north-south pair of lobes of the quadrupolar molecular outflow (Lee et al. 2002).

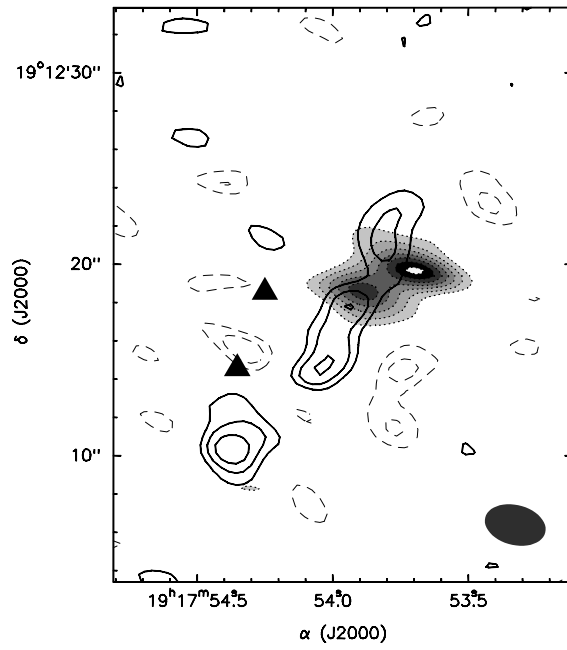


Fig. 6.— Contour map of the SiO 5–4 emission overlaid with the grey scale image of the 1.35 mm dust. Contours are  $-3$ ,  $-2$ ,  $2$ ,  $3$ ,  $4$  and  $5$  times  $0.05 \text{ Jy beam}^{-1}$ , the rms noise of the map. The synthesized beam is shown in the bottom right corner. The filled triangles mark H<sub>2</sub> knots (Palacios & Eiroa 1999).



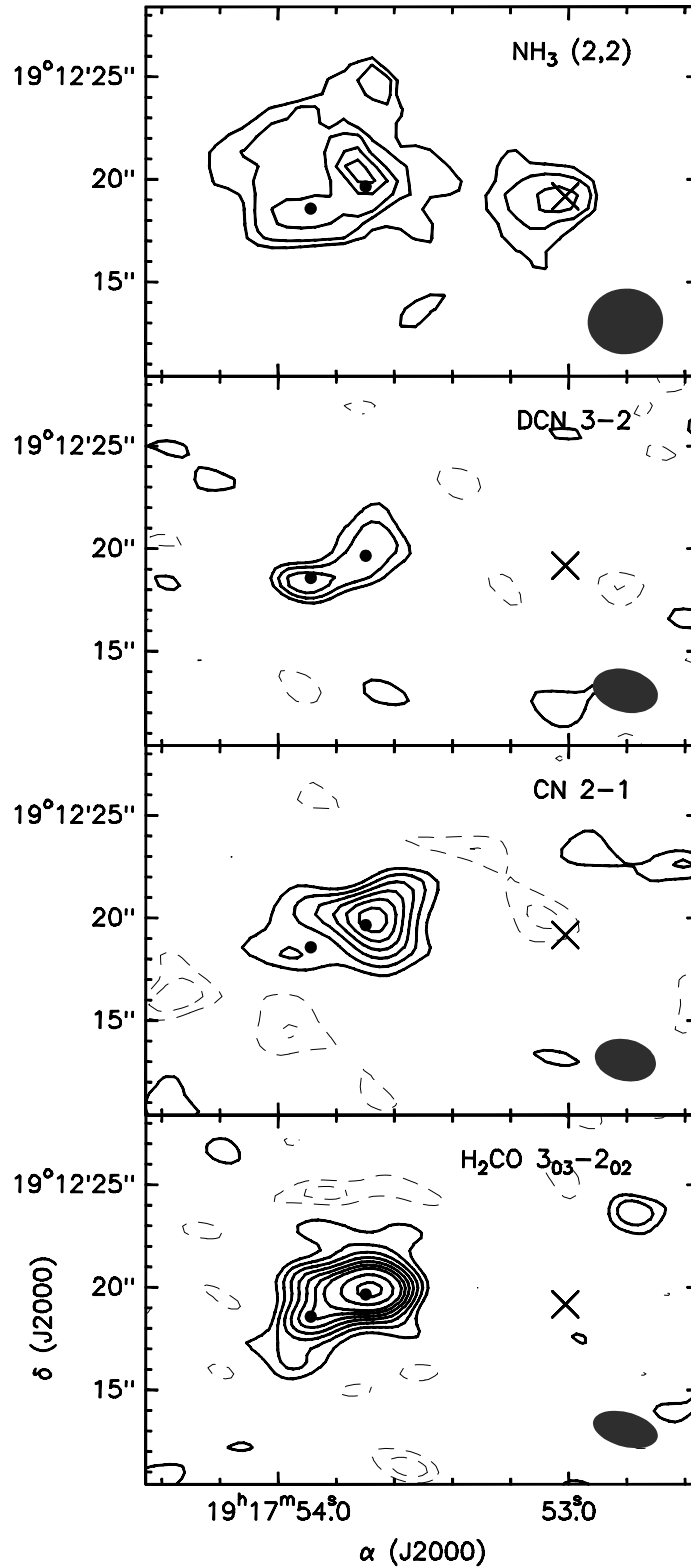


Fig. 7.— Integrated emission of the  $\text{H}_2\text{CO}$  3<sub>0,3</sub>-2<sub>0,2</sub>, CN 2-1, DCN 3-2 lines observed with the SMA. For comparison we have also included the integrated emission of the  $\text{NH}_3$  (2,2) line obtained with the VLA by Girart et al. (1997). The synthesized beams are shown in the lower right corner of each panel. Contours are  $-2, 2, 3, 4, 5, 6, 7, 8, 10$  and  $12$  times  $3.2, 34, 16$  and  $51$   $\text{mJy beam}^{-1} \text{ km s}^{-1}$  for  $\text{NH}_3$ , DCN, CN and  $\text{H}_2\text{CO}$ , respectively. The

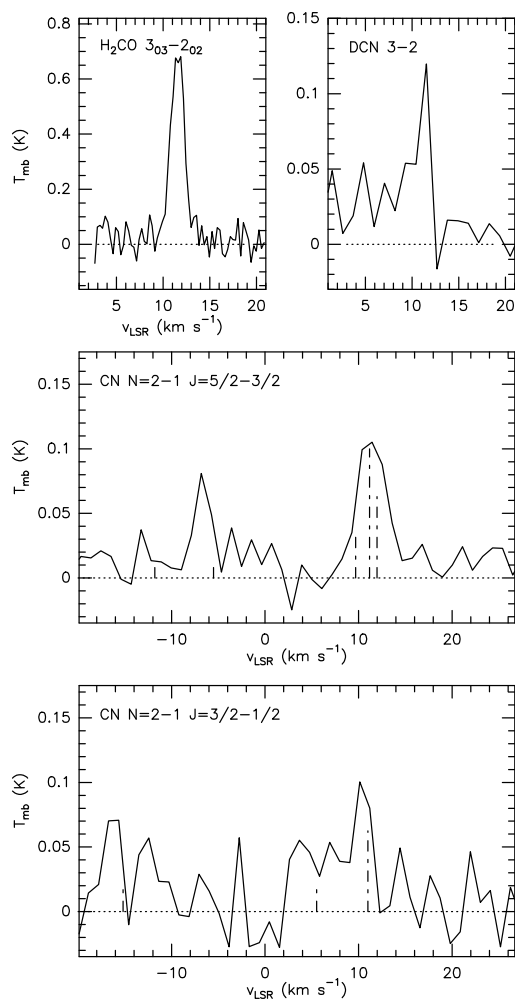


Fig. 8.— Spectra of the  $\text{H}_2\text{CO } 3_{0,3}-2_{0,2}$ ,  $\text{DCN } 3-2$ ,  $\text{CN } N=2-1, J=5/2-3/2$  and  $J=3/2-1/2$  obtained averaging a region of  $7'' \times 5''$  around SMA 1 and SMA 2. The CN and DCN spectra has a lower velocity resolution ( $\approx 1.0 \text{ km s}^{-1}$ ). For the CN hyperfine transitions, a vertical dashed line indicates the position of the expected hyperfine transition with the height proportional to its relative intensity.

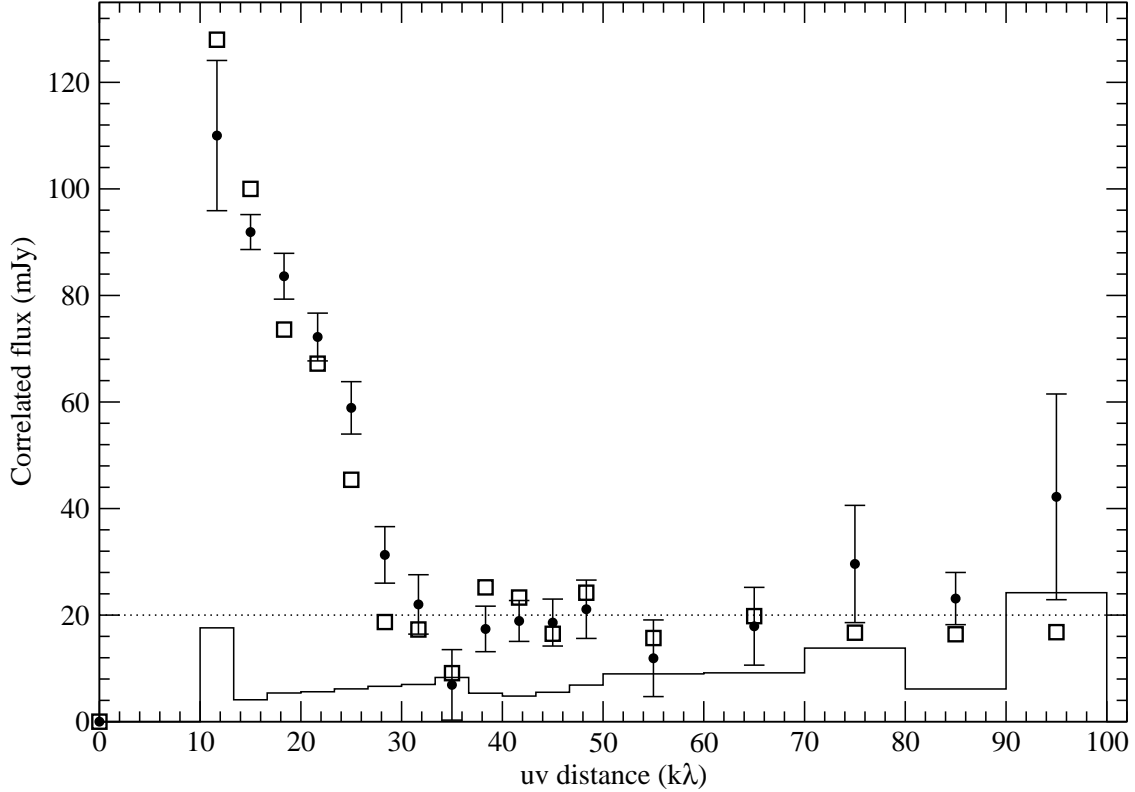


Fig. 9.— SMA correlated flux for the 1.35 mm continuum emission *versus* uv distance (in units of  $k\lambda$ ) at the position of SMA 2. The correlated flux was derived by vector averaging the amplitude of the visibilities over annular bins. The bins have a width of 3.3  $k\lambda$  for radius lower than 50  $k\lambda$  and of 10  $k\lambda$  for larger radii. The solid line shows the expected value for the amplitude assuming no signal (i.e., the "zero bias"). The dotted line shows the expected flux for an unresolved source of 20 mJy. The open squares show the expected correlated for the model  $T_0 = 20$  K and  $n_0(\text{H}_2) = 2.4 \times 10^6 \text{ cm}^{-3}$  described in § 4.1.

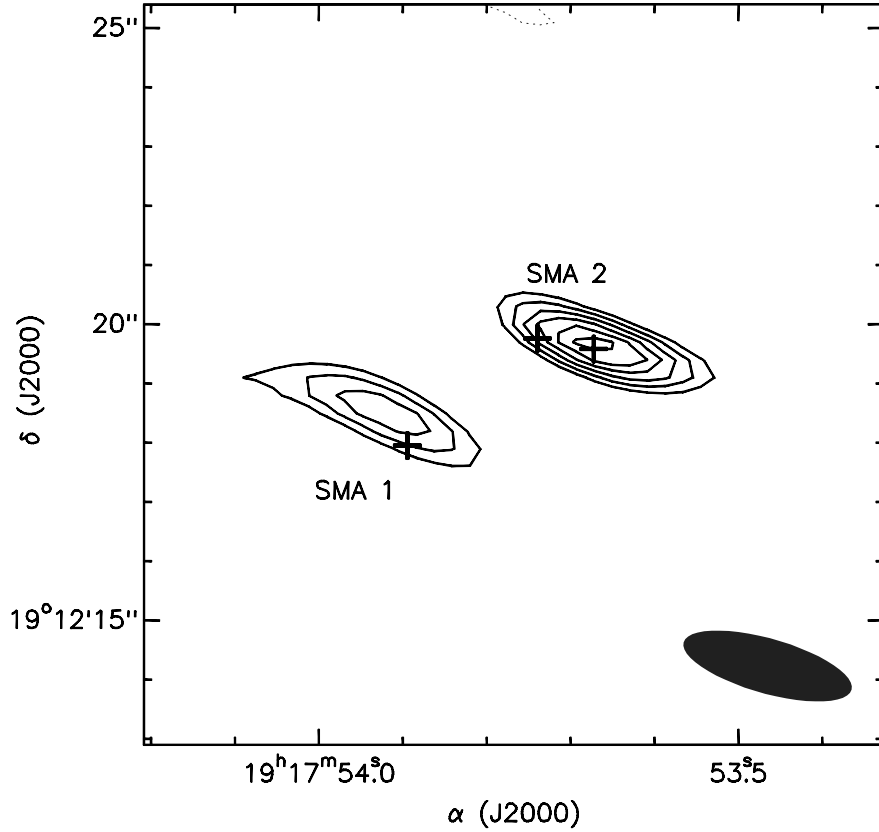


Fig. 10.— SMA map of the 1.35 mm dust emission obtained using only the visibilities with a radius larger than  $45 \text{ k}\lambda$  in the  $(u, v)$  plane and applying a Natural weighting to the visibilities. The contour levels are  $-3, 3, 4, 5, 6$  and  $7$  times the rms noise of the map,  $2.4 \text{ mJy beam}^{-1}$ . The synthesized beam,  $2''.94 \times 0''.92$  with a  $PA = 74.2^{\circ}$ , is shown in the bottom right corner. The crosses show the position of VLA 2A (the western cross) and VLA 2C, which are associated with SMA 2, and VLA 2D, associated with SMA 1.

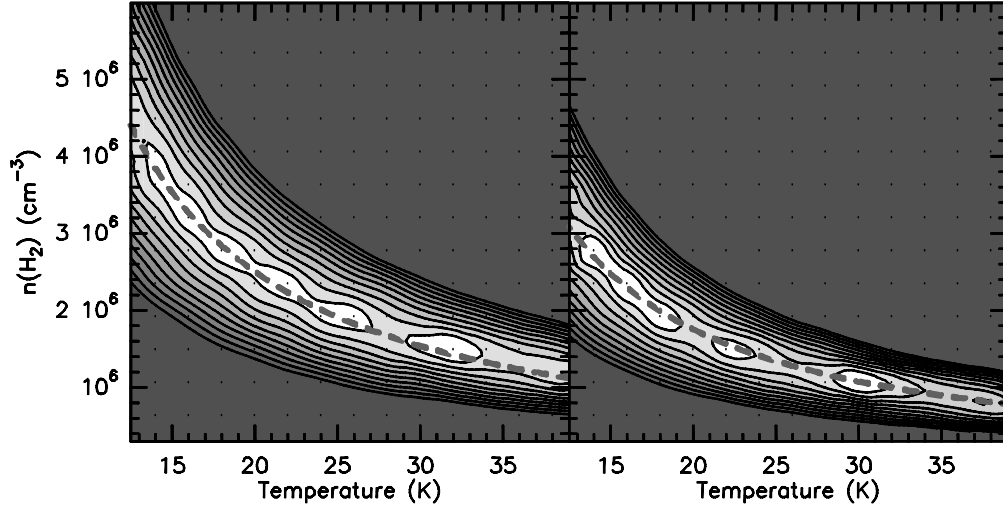


Fig. 11.— Plots shows the locus of best solutions represented by the function of the *rms* of the residual map derived by subtracting the dust model for an inner radius of 30 (*left panel*) an 100 AU (*right panel*) to the SMA visibility data of the 1.3 mm continuum emission. Levels are in steps of 3 times the *rms* of the original SMA map, 1.5 mJy beam<sup>-1</sup>. The dashed grey line shows the line of approximately set of best solutions represented as the function  $n(\text{H}_2) = 1.5 \times 10^6 [T/30 \text{ K}]^{1.2} \text{ cm}^{-3}$  (*left panel*) and  $n(\text{H}_2) = 1.1 \times 10^6 [T/30 \text{ K}]^{1.2} \text{ cm}^{-3}$  (*right panel*).

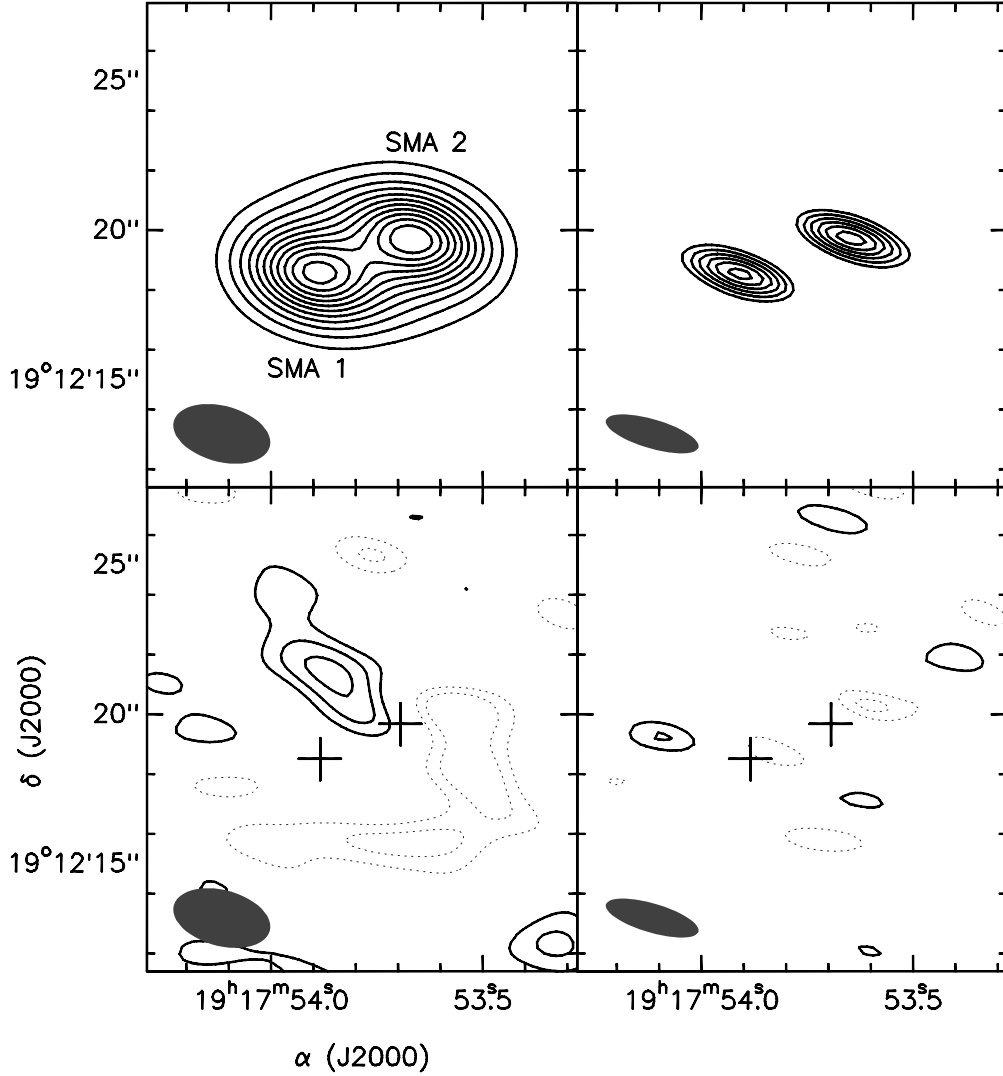


Fig. 12.— SMA synthetic maps for the dust model  $R_{\text{inner}} = 30$  AU,  $T_0 = 20$  K and  $n_0 = 2.4 \times 10^6 \text{ cm}^{-3}$  described in § 4.1. *Left panels:* the model (top) and residual (bottom) dust maps obtained using all the visibilities observed with the SMA and using robust of 1. Contour levels for the model map are  $-3, 3, 5, 7, \dots, 21$  times  $1.5 \text{ mJy beam}^{-1}$ , the  $rms$  of the map. Contour levels for the residual map are  $-3, -2, 2, 3,$  and  $4$  times  $1.5 \text{ mJy beam}^{-1}$ , *Right panels:* the model (top) and residual (bottom) dust maps obtained using visibilities with a radius larger than  $45 \text{ k}\lambda$  and Natural weighting (as in Fig. 10). Contour levels are  $-3, -2, 2, 3, 4, 5, 6$  and  $7$  times  $2.4 \text{ mJy beam}^{-1}$ . The synthesized beams are shown in the lower left corner of each panel. The crosses show the position of SMA 1 and SMA 2.

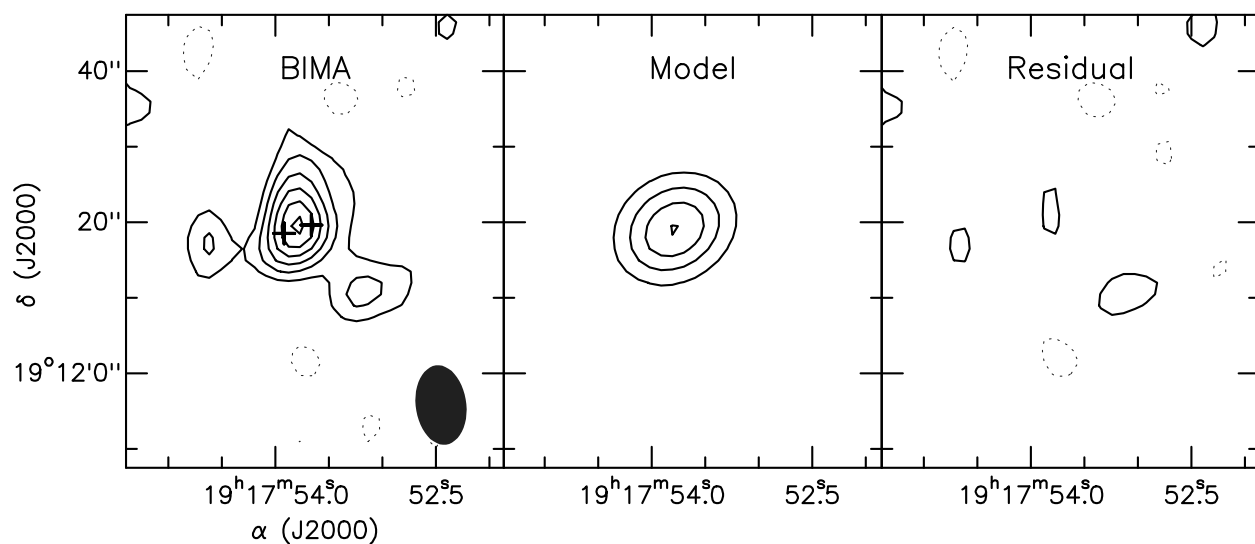


Fig. 13.— *Left panel:* BIMA map of the 3.2 mm continuum emission obtained with the C configuration in September 2003. The synthesized beam,  $10''.6 \times 6''.7$  and  $PA = -7^\circ$ , is shown in the bottom right corner. Contours are  $-2, 2, 3, 4, 5, 6$  and  $7$  times  $2.8 \text{ mJy beam}^{-1}$ , the rms noise of the map. The crosses show the position of SMA 1 and SMA 2. *Middle panel:* BIMA synthetic map at 3.2 mm continuum at the C configuration for the dust model  $T_0 = 20 \text{ K}$  and  $n(\text{H}_2)_0 = 2.4 \times 10^6 \text{ cm}^{-3}$  described in § 4.1. Contours are the same as in the previous panel. *Right panels:* BIMA residual map obtained from the previous two maps.

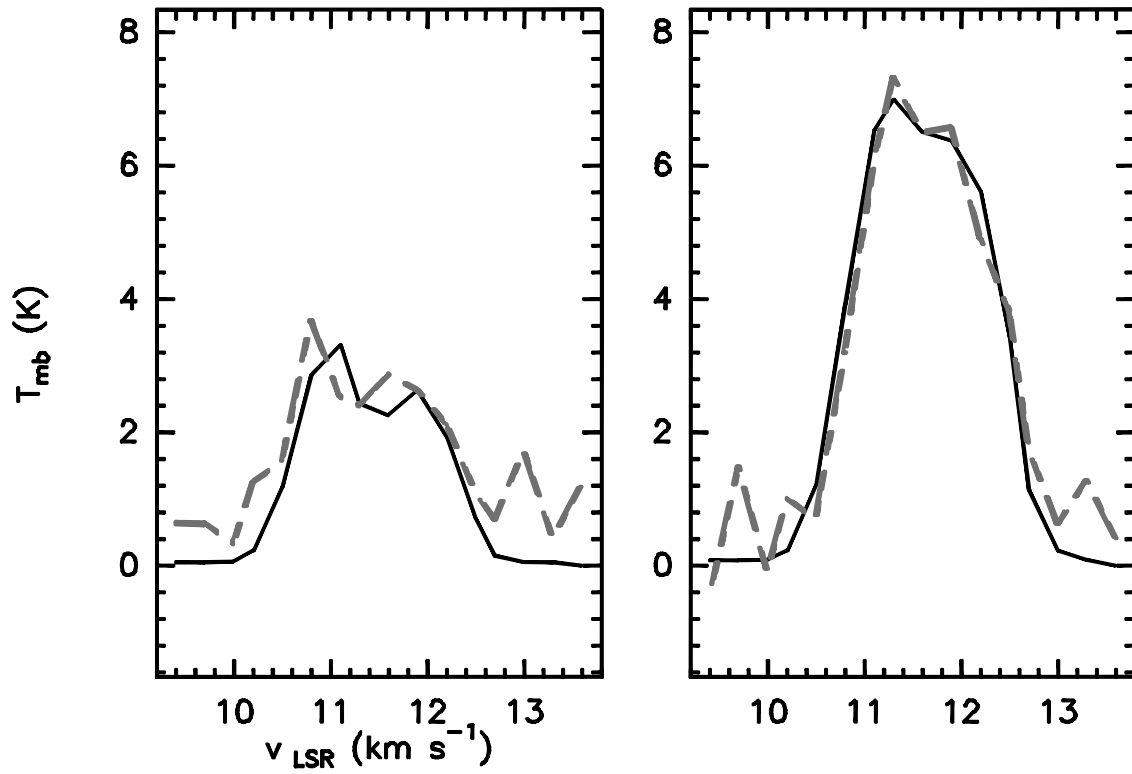


Fig. 14.— Synthetic (solid line) and observed (dashed grey line)  $\text{H}_2\text{CO } 3_{0,3}-2_{0,2}$  spectra at SMA 1 (left panel) and SMA 2 (right panel). The model parameters for the synthetic spectra are the same as in Figure 15.



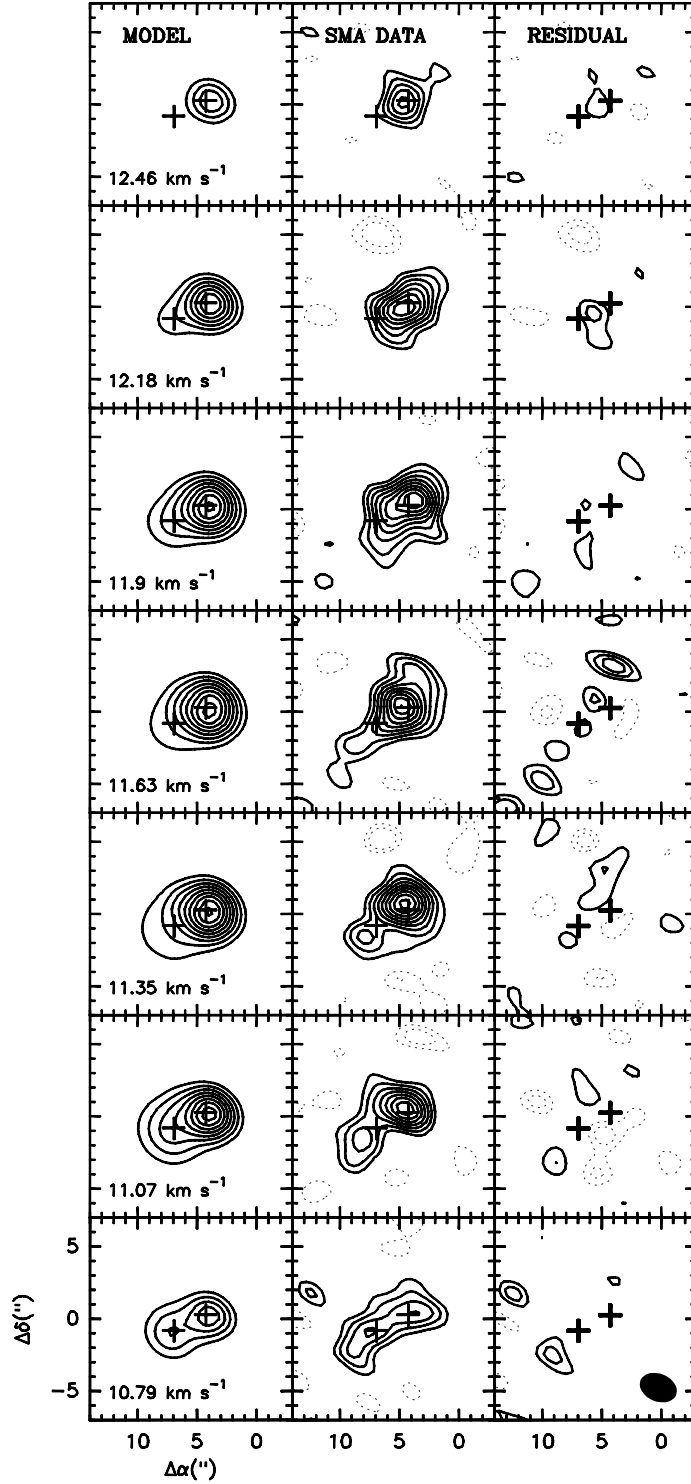


Fig. 15.— Channel maps of one of the best models, the SMA data and the residual (SMA–model) for the  $\text{H}_2\text{CO } 3_{0,3}\text{--}2_{0,2}$  emission. Contours are  $-3, -2, 2, 3, 4, 5, 6, 7$  and  $8 \times 0.17 \text{ mJy beam}^{-1}$ . The synthesized beam is shown in the lower right corner of the lower right panel. The crosses show the position of the dust sources SMA 1 and SMA 2. The parameters for this model are  $X[\text{p-H}_2\text{CO}] = 3 \times 10^{-9}$ ,  $R_{in} = 240 \text{ AU}$  and  $R_{out} = 600 \text{ AU}$  for SMA 2, and  $X[\text{p-H}_2\text{CO}] = 1 \times 10^{-10}$ ,  $R_{in} = 60 \text{ AU}$  and  $R_{out} = 5000 \text{ AU}$  for SMA 1. The  $v_{\text{LSR}}$  velocity of the channels is shown in the lower left corner of the right panels.

Table 1. Parameters of the SMA observations

Observation	$\nu$ (GHz)	Synthesized Beam		$\Delta\nu$ (MHz)	Spectral Resolution (km s <sup>-1</sup> )	<i>rms</i> Noise (mJy beam <sup>-1</sup> )
		HPBW (arcsec)	PA (deg)			
Continuum	222.31	$3.3 \times 1.5$	79	4000		1.8
H <sub>2</sub> CO 3 <sub>0,3</sub> -2 <sub>0,2</sub>	218.2222	$3.1 \times 1.8$	76	104	0.28	175
DCN 3-2	217.2385	$3.2 \times 2.1$	76	104	1.07	78
SiO 5-4	217.1050	$3.2 \times 2.1$	76	104	1.12	60
CN 2-1 5/2-3/2 7/2-5/2 <sup>a</sup>	226.8748	$3.1 \times 2.0$	76	104	1.07	65
CN 2-1 3/2-1/2 5/2-3/2 <sup>a</sup>	226.6595	$3.1 \times 2.0$	76	104	1.07	88

<sup>a</sup>CN N,J,F hyperfine transitions

Table 2. Dust properties at 1.35 mm<sup>a</sup>

Source	Positions		$I_\nu$ (mJy beam <sup>-1</sup> )	$S_\nu$ (mJy)	Deconvolved Size (arcsec)	PA (deg)
	$\alpha$ (J2000)	$\delta$ (J2000)				
SMA 1	19 <sup>h</sup> 17 <sup>m</sup> 53 <sup>s</sup> .884	19°12'18".51	29.9±1.8	45±4	(2.0 ± 0.3) × (< 0.6)	56 ± 9
SMA 2	19 <sup>h</sup> 17 <sup>m</sup> 53 <sup>s</sup> .694	19°12'19".68	33.7±1.8	59±4	(2.3 ± 0.2) × (1.0 ± 0.2)	73 ± 6

<sup>a</sup>Values corrected by the primary beam of the SMA antennas.

Table 3: Masses of the different components in L723

Source	$S_\nu(1.35\text{mm})$ (mJy)	$T_{\text{dust}}$ (K)	$M$ ( $M_\odot$ )
All <sup>a</sup>	128±6	25	0.24
SMA 1	45±4	25	0.09
SMA 2	59±4	25	0.11
WHS	≤ 5.7	25	≤ 0.011

<sup>a</sup> To estimate the total mass we took into account the contribution of the mass from the 24 mJy excess of emission of the Natural map (obtained adopting a temperature of 20 K).

Table 4: H<sub>2</sub>CO 3<sub>0,3</sub>-2<sub>0,2</sub>

Source	$I_\nu$ (K)	$\int I_\nu dv$ (K km s <sup>-1</sup> )	$v_{\text{LSR}}$ (km s <sup>-1</sup> )	$\Delta v$ (km s <sup>-1</sup> )
SMA 1	4.0±0.7	8.7±1.0	11.47±0.11	2.0±0.3
SMA 2	8.7±0.7	14.6±0.8	11.64±0.04	1.6±0.1

Table 5: Best H<sub>2</sub>CO Models

Source	$X[\text{p-H}_2\text{CO}]$	$R_{in}$ (AU)	$R_{out}$ (AU)
SMA 1	$(8-30) \times 10^{-11}$	30–120	600–5000
SMA 2	$(3-10) \times 10^{-10}$	30–240	300–600